HHS Public Access

Author manuscript

Phys Med Biol. Author manuscript; available in PMC 2017 September 21.

Published in final edited form as:

Phys Med Biol. 2016 September 21; 61(18): 6821–6832. doi:10.1088/0031-9155/61/18/6821.

Mechanical analysis of an axially symmetric cylindrical phantom with a spherical heterogeneity for MR elastography

Benjamin L Schwartz[#1], **Ziying Yin**[#1], and **Richard L Magin**[1]

[1] Department of Bioengineering, University of Illinois at Chicago, 851 S Morgan St, 218 SEO, Chicago, IL 60607, USA

[#] These authors contributed equally to this work.

Abstract

Cylindrical homogenous phantoms for magnetic resonance (MR) elastography in biomedical research provide one way to validate an imaging systems performance, but the simplified geometry and boundary conditions can cloak complexity arising at tissue interfaces. In an effort to develop a more realistic gel tissue phantom for MRE, we have constructed a heterogenous gel phantom (a sphere centrally embedded in a cylinder). The actuation comes from the phantom container, with the mechanical waves propagating toward the center, focusing the energy thus allowing for the visualization of high-frequency waves that would otherwise be damped. The phantom was imaged and its stiffness determined using a 9.4 T horizontal MRI with a custom build piezo-elastic MRE actuator. The phantom was vibrated at three frequencies, 250, 500, and 750 Hz. The resulting shear wave images were first used to reconstruct material stiffness maps for thin (1 mm) axial slices at each frequency, from which the complex shear moduli μ were estimated, and then compared with forward modeling using a recently developed theoretical model who took μ as inputs. The overall accuracy of the measurement process was assessed by comparing theory with experiment for selected values of the shear modulus (real and imaginary parts). Close agreement is shown between the experimentally obtained and theoretically predicted wave fields.

1. Introduction

Many pathologies can be characterized by the changes they induce in the mechanical properties of tissue, e.g. cirrhotic liver is stiffer than healthy liver. This phenomenon has been exploited by physicians, since antiquity, to diagnose disease through the technique of palpation, wherein the physician manually feels for heterogeneities in a region of a patient's body by applying pressure thereupon. The obvious limitations of this are that an abnormally stiff or soft region can be missed if it is too deep in the body and that the sense of touch of a doctor is highly subjective. Dynamic elastography seeks to answer this need, allowing for the non-invasive viscoelastic description of soft tissues by measuring the displacement fields from an applied stress [1]. In MR elastography (MRE) [2, 3, 4, 5, 6] a harmonic shear wave is introduced into the tissue by an internal or external actuator. The MRE motion-encoding

benjithegreat@asu.edu, yin.ziying@mayo.edu, and rmagin@uic.edu

gradients are synchronized with the mechanical actuator. The protons in these oscillating magnetic field accrue a phase shift corresponding to their displacement. The phase contrast image is analogous to a wave image from which the mechanical properties of the tissue, e.g. shear modulus, can be calculated. As with any imaging modality, phantom studies have been used to optimize MR elastography.

1.1. Elastography Phantoms

Researchers choose their elastography phantoms' materials and geometry based on e.g. what rheological phenomenon they want to model or what reconstructive algorithm they will use. Royston et al [7] and Yaşar et al [8] designed a phantom that is stimulated by vibrating, along the central axis, the cylindrical container in which the tissue-mimicking material is held, as opposed to Okamoto et al [9] whose actuation came from within the material. The incident wave is geometrically focused as it travels toward the radial center, where it finally, due to the spatial concentration of the mechanical energy, will increase in amplitude, overcoming the attenuation due to viscous damping. That is, the geometric focusing allowed the displacement to be discernible deep in the center of the phantom, far from the harmonic forced oscillation, even at high frequencies ($< 1.6 kHz$). Yaşar et al [10] and Liu et al [11] used these cylindrical phantoms to characterize the viscoelastic model of a silicone rubber from the complex shear moduli over a wide range of frequencies showing that fractional order models capture best the complicated nature of viscoelastic material. Schwartz et al [12] generalized those works in a geometric sense, studying a heterogeneous phantom composed of two concentric cylinders of hydrogel. Klatt et al introduced the so-called SLIM-MRE, wherein three displacement projections are simultaneously encoded into the MR phase signal, using these cylindrical phantoms which had one [13] and three [14] spherical hydrogel heterogeneities embedded in a stiffer hydrogel matrix. Yin et al [15] also used a cylindrical phantom with a single spherical heterogeneity in their work demonstrating the feasibility of combining the data acquisition for diffusion-weighted imaging and MR elastography into a single scan, so-called diffusion-MRE, while Yaşar et al [16], with a similar phantom, showed how to encode three excitation frequencies at once, each spatial encoding direction—read, phase, and slice—being devoted to a single frequency.

Spherical heterogeneities were used in [13, 14, 15, 16] because they are affordable, readily available and easily embedded in the cylindrical matrix without introducing unwanted heterogeneities, e.g. bubbles of air, but they have a clinical relevance as well, e.g. osteoarthritis treatment [17]. MRI techniques [18] and in particular MR elastography [19] have been used to characterize the growth and development of artificial tissue constructs; so, Yin et al [20] investigated the potential of using the complex shear modulus obtained in MRE as a biomarker for alginate beads, embedding three spheres in their cylindrical phantoms.

1.2. Objective

Since the cylindrical phantom with embedded spherical heterogeneities plays an important role in the research and development of MR elastography, it is vital that it be carefully rigorously mathematically modeled, elucidating its mechanical behavior. Therefore, in a two-part study (of which this is the 2nd), we set out to model analytically, and conduct a

theoretical and experimental study of, the scattering and diffraction of axially-symmetric, radially-converging, cylindrical waves by a viscoelastic sphere. In an earlier companion work, Schwartz et al [21] present the entire, first-principle derivation, solution, and numeric examples of the problem of a sphere embedded with welded contact in an oscillating infinite circular cylinder. In this experimental study we describe the mathematical theory (briefly), phantom construction, image acquisition, and parameter estimation techniques. We compare experimental and theoretical results and consider future research directions.

2. Theory

We mathematically model the phantom as an infinitely long circular cylindrical tube that is filled with a viscoelastic solid, referred to as medium 1. A spherical viscoelastic solid, medium 2, is embedded in the center of medium 1, i.e the center of the sphere lies on the axis of the cylindrical tube. We define the spherical heterogeneity and surrounding region, respectively, by spherical (r, θ, ϕ) and cylindrical coordinates (ρ, z, ϕ), shown in figure 1. The $\hat{z}$ axis is aligned with the axis of the tube and contains the center of the spherical inclusion. The two media have different shear stiffnesses. The rigid tube harmonically oscillates along the cylindrical $\hat{z}$ axis and we assume that medium 1 is in welded contact with both boundaries. The displacement of the two media satisfy the vector Helmholtz equation,

$$\alpha_i^2 \nabla\nabla\cdot\overrightarrow{U} - \beta_i^2 \nabla\times\nabla\times\overrightarrow{U} + \omega^2\overrightarrow{U} = 0 \quad (1)$$

where

$$\alpha_i^2 = (\lambda_i + 2\mu_i)\,\gamma_i^{-1} \quad (i=1,2) \quad (2a)$$

$$\beta_i^2 = \mu_i \gamma_i^{-1} \quad (i=1,2) \quad (2b)$$

The constants λ_i and μ_i are the Lame constants, and γ_i is the density of the material. Here the index i is 1 or 2 to denote the medium. Throughout this analysis we suppress the harmonic time dependence, e^{iwt}. Due to the axial symmetry of our system, we may neglect all components and dependencies of the azimuthal direction, ϕ. The assumption of intimate contact between medium 1 and the boundaries means we will enforce equality of displacement at the tube wall and equality of displacement and stress at the spherical radius. Mathematically the conditions at $\rho = b$ are given as

$$u_{1\rho}(\rho, z)\,|_{\rho=b} = 0, \quad (3a)$$

$$u_{1z}(\rho, z)|_{\rho=b} = GB_w(z) \quad (3b)$$

where G is the amplitude of the forced oscillations and $B_w(z)$ is the boxcar function [22]. Here $u_{1\rho}$ and u_{1z} are, respectively, the magnitudes of the ρ and z components of the displacement vector, $\overrightarrow{U}$, in the cylindrical coordinates. At $r = a$, we have

$$u_{1r}(r, \theta)|_{r=a} = u_{2r}(r, \theta)|_{r=a}, \quad (4a)$$

$$u_{1\theta}(r, \theta)|_{r=a} = u_{2\theta}(r, \theta)|_{r=a}, \quad (4b)$$

$$\sigma_{1rr}(r, \theta)|_{r=a} = \sigma_{2rr}(r, \theta)|_{r=a}, \quad (4c)$$

$$\sigma_{1r\theta}(r, \theta)|_{r=a} = \sigma_{2r\theta}(r, \theta)|_{r=a}. \quad (4d)$$

where u_{1r} and $u_{1\theta}$ are, respectively, the magnitudes of the r and θ components $\overrightarrow{U}$ in spherical coordinates and σ_{1rr} and $\sigma_{1r\theta}$ are the magnitudes of the rr and $r\theta$ components of the stress tensor. We identify three wave fields in our system, the incident, scattered, and refracted fields. The incident field is a cylindrical wave that travels from the inner radius of the tube, converging radially toward the center. The scattered and refracted fields are spherical waves that respectively reflect off and are transmitted through the spherical inclusion. Each wave field can be defined in terms of its longitudinal, $\overrightarrow{L}$, and vertically-polarized transverse components, $\overrightarrow{N}$, given as

$$\overrightarrow{L} = \nabla\Phi, \quad (5)$$

$$\overrightarrow{N} = \beta_i^{-1}\nabla \times \nabla \times \hat{e}\mathrm{X}, \quad (6)$$

where each potential function, Φ and X, solves the scalar Helmholtz equation,

$$\left(\nabla^2 + \left\{\alpha_i^{-2}, \beta_i^{-2}\right\}\right)\{\Phi, \mathrm{X}\} = 0, \quad (5)$$

and the vector, $\hat{e}$, depends on the coordinate system [23]. In cylindrical coordinates $\hat{e} = \hat{z}$, and in spherical coordinates $\hat{e} = r\hat{r}$ [24]. The axially symmetric nature of our problem means the wave fields have no horizontally-polarized transverse component. We may now define the magnitudes of the cylindrical (cyl) displacement and spherical (sph) displacements and stresses in terms of the scalar potential functions. They are given, in terms of the scalar potential functions, as [24]

$$u_\rho = \frac{\partial \Phi_{cyl}}{\partial \rho} + \frac{1}{q_i}\frac{\partial^2 \mathrm{X}_{cyl}}{\partial \rho \partial z}, \quad (6a)$$

$$u_z = \frac{\partial \Phi_{cyl}}{\partial z} + \frac{1}{q_i \rho}\frac{\partial}{\partial \rho}\left(\rho \frac{\partial \mathrm{X}_{cyl}}{\partial \rho}\right) \quad (6b)$$

$$u_r = \frac{\partial \Phi_{sph}}{\partial r} + \frac{1}{q_i}\left(\frac{\partial^2 r\mathrm{X}_{sph}}{\partial r^2} - \nabla^2 \mathrm{X}_{sph}\right) \quad (6c)$$

$$u_\theta = \frac{1}{r}\frac{\partial \Phi_{sph}}{\partial \theta} + \frac{1}{r}\frac{\partial^2 r\mathrm{X}_{sph}}{\partial r \partial \theta}, \quad (6d)$$

with the stress components given in terms of the displacements,

$$\sigma_{rr} = \lambda\left(\frac{\partial u_r}{\partial r} + \frac{1}{r}\frac{\partial u_\theta}{\partial \theta} + 2\frac{u_r}{r} + \frac{cot\,(\theta)}{r}u_\theta\right) + 2\mu\frac{\partial u_r}{\partial r}, \quad (7a)$$

$$\sigma_{r\theta} = \mu\left(\frac{1}{r}\frac{\partial u_r}{\partial \theta} - \frac{u_\theta}{r} + \frac{\partial u_\theta}{\partial r}\right). \quad (7b)$$

3. Methods

3.1. Phantom Preparation

For a general frame of reference, magnitude MR images of the two phantoms used in this study are shown in figure 2. The slight curvature on the bottom of the coronal images of both phantoms are imaging artifacts due to heterogeneities in the main magnetic field of the MRI scanner. The phantoms are actually flat in those regions.

3.1.1. Homogenous Phantom—The phantom matrix was made from a mixture of agarose (SeaKem LE Agarose, Lonza, Rockland, ME) 0.75% by weight, and food grade

gelatin (Knox Original Unflavored Gelatine, Kraft Foods Group Inc., Northfield, IL), 4% by weight, in water. The solution was heated until clarification occured at 90 °C. The molten gel was poured into a cylindrical container made of an acetyl resin (Delrin, DSM Engineering Plastic Products, Inc., Reading, PA), and allowed to solidify at room temperature for 12 hours before being scanned.

3.1.2. Heterogenous Phantom—The heterogeneous phantom is identical to the homogeneous phantom save for the addition of a 1.7 cm diameter soft spherical inclusion. The procedure for making the surrounding agarose/gelatin gel (medium 1) is the same as presented above. The spherical inclusion (medium 2) was formed from dehydrated beads (Rainbow Water Beads, Greenville, SC) by immersion in distilled water for 8 hours. They are composed of a liquid crystalline polymer that absorbs water to form spherical beads of a hydrated gel. An individual bead was embedded in the center of the agarose/gelatin gel in the cylindrical container and allowed to gel at room temperature for 12 hours prior to the start of scanning.

3.2. Experimental Setup

MR elastography experiments were performed at 9.4 T using a horizontal bore Agilent small-animal MR scanner (310/ASR, Agilent Technologies, Santa Clara, CA). A 39 mm diameter quadrature RF coil was used inside a 60 mm diameter gradient coil with a maximum gradient of 1000 G/m. The gel-filled container was placed horizontally inside the center of the RF coil. the container was attached to a pre-loaded piezo-actuator (p-840.1, PhysikInstrumente (PI) GmbH & Co. KG, Germany), which generates the transverse vibration motion. All phantoms were scanned at the excitation frequencies of 250, 500, and 750 Hz. This experimental setup establishes concentric wave patterns within the gel.

3.3. Data Acquisition

A customized spin-echo (SE) based MR elastography sequence with a sinusoidal motion-sensitizing gradient (MSG) was used for data acquisition, obtaining one central axial slice and one central coronal slice. The acquisition parameters were as follows: repetition time (TR) = 1 s, echo time (TE) = 28 ms, field of view (FOV) = 4 cm × 4 cm, matrix size = 128 × 128, slice thickness = 1 mm, MSG = 30 G/cm. In order to keep the same SNR at different frequencies, the number of MSG cycles varied with the actuation frequency from 2 to 6 to accommodate constant TR/TE imaging parameters. For example, we used 2 MSG cycles at 250 Hz, 4 MSG cycles at 500 Hz, and 6 MSG cycles at 750 Hz, which all lead to an MSG duration of 8 ms. In all scans, the MSG was applied along the principle direction of vibration in our experimental setup. Phase difference images were made from two acquisitions by inverting the polarity of the MSG. Four time steps were acquired per actuation cycle.

3.4. Data Processing

The raw phase images were unwrapped if wrapping artifacts were present, and Fourier transformed along the time axis over four time steps. The resulting complex wave images for each driving frequency were spatially filtered for noise reduction using a Gaussian filter. The filter kernel size is 128 × 128, and the cutoff frequency for this high-pass filter is 160 Hz.

The wavelengths, l_i, were estimated using a 2D local frequency estimation (LFE) algorithm applied to the wave images [25]. The shear stiffness maps were calculated from the following relation [26]

$$\mu_i = \gamma_i (l_i f)^2. \quad (8)$$

We assume γ_i to be the same as water, i.e. 1000 kg/m^3. At each frequency, the shear stiffness values were spatially averaged over regions of interest (ROIs) prescribed by the boundaries of the spherical inclusion visible in the MR elastography magnitude image or, in the case of the cylindrical phantom, by selection the region over the entire sample. The mechanical inputs for the theoretical forward modeling were estimated from the experimental results. The storage modulus, $\Re\mathfrak{e}\mu_i$, was obtained from the LFE while the loss modulus, $\Im\mathfrak{m}\mu_i$, was determined by trial-and-error comparisons of theoretical and experimental images, manually adjusting the value to optimize the fit of the normalized displacement. The complex shear moduli used as inputs for the forward modeling to create the theoretical wave fields are summarized in Table 1. The agreement between the experimentally obtained wave fields, $\vec{U}_{MRE}$, and those theoretically predicted, $\vec{U}$, is assessed both qualitatively, by visual comparison of the axial and coronal views of the wave fields as well as their linear profiles, and quantitatively, by calculating from the line profiles the root mean square error, RMSE, given here as

$$RMSE = \sqrt{\frac{\sum_{\mathfrak{n}=1}^{n} \left(\vec{U}_{\mathfrak{n}} - \vec{U}_{MRE,\mathfrak{n}} \right)^2}{n}}, \quad (9)$$

where $n = 128$ for all profile comparisons. All theoretical calculations were done on the computational software, Mathematica (Version 9, Wolfram Research, Inc., Champaign, IL). With our Mathematica code it took approximately 2 hours to render a 250 Hz wave field using a desktop computer running Windows 7 Ultimate–the processor was an Intel®Core™i5-2500K central processing unit at 3.30 GHz, with 7.71 usable GB of installed memory, and a 64-bit operating system–while a 750 Hz image took over 8 hours. For comparison, the normalized analytic linear profiles were taken out of the experimental MR elastography wave image and the corresponding simulated wave image.

4. Results

We compare the experimental and theoretical displacement wave fields at three excitations frequencies, 250, 500, and 750 Hz. We're limited to this range because too low of a frequency would yield wavelengths bigger then the phantom diameter and too high of a frequency would make the solution's computation time untenable. It is related to the degree of truncation N which is informed by the number of wavelengths within the field of view and is proportional to $\frac{2\pi}{\lambda}$, where λ is the shear wavelength. For the homogenous phantom, figure 3 shows the analytic and experimental normalized displacements as seen in in the coronal plane through the center of the cylinder and through the axial plane at the level of

the dashed lines in the coronal images. Figure 4 has the analogous results for the heterogeneous phantom. In figure 5 the theoretical displacements along the dashed lines in axial images are superimposed on the experimental displacements. The RSME for each of the phantoms at every frequency is summarized in table 2. They serve as a benchmark of model agreement for future studies. Figure 6 shows the elastorams of the homogenous (top) and heterogenous (bottom) phantoms calculated from the experimentally obtained axial wave images in figure 3 and figure 4, respectively. These spatial distributions of the storage modulus are given in units of kPa.

5. Discussion

The point of these two papers (the present one and it's companion Ref. [21]) is that by analytically modeling this heterogeneous body we broaden the theoretical framework through which it is understood, which could allow to identify the impact of the shortcomings of conventional reconstruction algorithms, e.g. LFE which fails to account for mode conversions. In LFE the shear modulus is estimated from the apparent wave length (see Eq. (8)) without distinguishing what wave fields are responsible for it. At an interface between two elastic media an elastic wave will undergo a mode conversion, e.g. when an incident transverse wave hits a boundary between two solids of differing stiffnesses, some of that energy will be scattered back from the boundary and some will refract through into the other medium. If the incident angle of the wave is not normal to the boundary, then both the scattered and refracted fields will have both transverse and longitudinal components and be the shape of the scatterer. LFE assumes that at each pixel the traveling wave is a plane wave. It is important to know what impact those assumptions have on parameter estimation.

In the coronal view of the simple cylinder phantom (figure 3) we see that the vertically polarized waves wave fronts are not parallel as the closed form analytic solution predicts they should be. This is more pronounced at the lower frequency, 250 Hz, than at 500 and 750 Hz. However, as the frequency goes up, the edge effects play a larger role, i.e. the waves become distorted at the top and bottom of the cylinder. That highlights the key shortcoming of this model: assuming an infinitely long cylinder. This limits the predictive use of our model to the central region, clearly shown by the agreement found in the axial view (figure 3) and the linear profiles (figure 5). Even in that region, though, there is not perfect consensus between theory and experiment. This is probably due to errors in estimation of the material's shear moduli, which are the inputs for the forward problem. Still, though, it is the outer part of both phantoms, i.e. outside the central region, where the theory and experiment fall out of agreement. It is true for both the homogenous and heterogenous phantoms.

As with the simple cylinder, in the case of the sphere embedded in a cylinder we find good agreement between the predicted wave field of the analytic solution and the experimentally obtained one, in the axially and radially central region. Again, the axial images and line profiles show this phenomenon (figure 4 and figure 5, respectively). Boumdary effects likely play a role in distorting the wave from the ideal, but in the heterogenous phantom there are two opportunities for miss characterizing the shear moduli inputs, namely the embedding gel and the spherical heterogeneity. Adjusting, for instance, $\Im\mathrm{m}\mu_2$, when solving the forward

problem to better match the experimental data will change the entire linear profile as the displacement of each region depends on the shear moduli of *both* regions [21].

Let us now consider some of the major limitations of this study. We assume the cylinder to be infinitely long but it is possible to model the cylinder as being finite in length using the methods employed by Kubenko and Savin [28]. We also assumed axial symmetry which, by inspection of figure 2, it's clear we didn't quite attain. Olsson [29] gives an analytic procedure, accounting for azimuthal dependence, that is applicable here. Finally, most of the discrepancy between theory and experiment is probably due to the inverse modeling estimates of the μ. An avenue for parameter estimation worth considering is the new method of O'Neill et al [30] that applies ordinary least squares regression and the Levenberg-Marquardt algorithm to linear, stationary, partial differential equations, with which both real and imaginary components of the μ can be estimated from the complex displacement data.

Future work will include formulating the mathematics so that we may use this phantom for inverse modeling, thus allowing us to investigate the behavior of a wider range of viscoelastic materials. Also, given the recent interest in the fractional calculus in the context of bioengineering [31], we will generalize the calculus operations in Eq.(1), i.e. replacing ∇ with ∇^{α}, where $0 < \alpha < 1$ is the order of differentiation [32].

Acknowledgments

We would like to thank Kevin Lynch (LAS) and Dave Mecha (COE), University of Illinois at Chicago, for their careful and precise machine work. We also extend our thanks to Coco Pinedo, Amber Pakos, and Colin Johnson for their thoughtful and stimulating comments. This work was supported by a grant from the National Institutes of Health, No. EB007537.

References

1. Sarvazyan A, Hall TJ, Urban MW, Fatemi M, Aglyamov SR, Garra BS. An overview of elastography–an emerging branch of medical imaging. Curr. Med. Imaging Rev. 2011; 7:255–82. [PubMed: 22308105]
2. Muthupillai R, Lomas DJ, Rossman PJ, Greenleaf JF, Mancuda A, Ehman RL. Magnetic resonance elastography by direct visualization of propagating acoustic strain waves. Science. 1995; 269:1854–57. [PubMed: 7569924]
3. Muthupillai R, Ehman RL. Magnetic resonance elastography. Nat. Med. 1996; 2:601–3. [PubMed: 8616724]
4. Walker CL, Foster FS, Plewes DB. Magnetic resonance imaging of ultrasonic fields. Ultrasound in Med. & Biol. 1998; 24:137–42. [PubMed: 9483781]
5. Othman SF, Xu H, Royston TJ, Magin RL. Microscopic magnetic resonance elastography (μMRE). Magn. Res. Med. 2005; 54:605–15.
6. Othman SF, Zhou XJ, Xu H, Royston TJ, Magin RL. Error propagation model for microscopic magnetic resonance elastography shear-wave images. Magn. Reson. Imaging. 2007; 25:94–100. [PubMed: 17222720]
7. Royston, TJ.; Yaşar, TK.; Magin, RL. Geometric focusing of high frequency shear waves for non-invasive high resolution MR elastography. Proc. 19th Annu. Meeting ISMRM.; Montreal, Canada. 07-13 May; 2011. p. 3481
8. Yaşar, TK.; Royston, TJ.; Magin, RL. Taking MR elastography (MRE) to the microscopic scale (μMRE). Proc. IEEE Int. Symp. on Biomedical Imaging: from Nano to Macro.; Chicago, IL. 30 March - 2 April; 2011. p. 1618-23.

9. Okamoto RJ, Clayton EH, Bayly PV. Viscoelastic properties of soft gels: comparison of magnetic resonance elastography and dynamic shear testing in the shear wave regime. Phys. Med. Biol. 2011; 56:6379–400. [PubMed: 21908903]
10. Yaşar TK, Magin RL, Royston TJ. Wideband MR elastography for viscoelasticity model identification. Magn. Reson. Med. 2013; 70:479–89. [PubMed: 23001852]
11. Liu Y, Yaşar TK, Royston TJ. Ultra wideband (0.5 – 16*kHz*) MR elastography for robust shear viscoelasticity model identification. Phys. Med. Biol. 2014; 59:7717–34. [PubMed: 25419651]
12. Schwartz BL, Yin Z, Yaşar TK, Liu Y, Khan AA, Ye AQ, Royston TJ, Magin RL. Scattering and diffraction of elastodynamic waves in a concentric cylindrical phantom for MR elastography. IEEE Trans. Biomed. Eng. 2016 in press.
13. Klatt D, Yaşar TK, Royston TJ, Magin RL. Sample interval modulation for the simultaneous acquisition of displacement vector data in magnetic resonance elastography: theory and application. Phys. Med. Biol. 2013; 58:8663–75. [PubMed: 24256743]
14. Klatt, D.; Yaşar, TK.; Royston, TJ.; Magin, RL. Introduction fo sample interval modulation for the simultaneous acquisition of 3D displacement data in MR elastography. Proc. 21st Annu. Meeting ISMRM.; Salt Lake City, UT. 20-26 April; 2013. p. 2444
15. Yin Z, Magin RL, Klatt D. Simultaneous MR elastography and diffusion acquisitions: diffusion-MRE (dMRE). Magn. Reson. Med. 2014; 71:1682–8. [PubMed: 24648402]
16. Yaşar TK, Klatt D, Magin RL, Royston TJ. Selective spectral displacement projection for multifrequency MRE. Phys. Med. Biol. 2013; 58:5771–81. [PubMed: 23912182]
17. Almqvist KF, Dhollander AAM, Verdonk PCM, Forsyth R, Verdonk R, Verbruggen F. Treatment of cartilage defects in the knee using alginate beads containing human nature allogenic chondrocytes. Am. J. Sports Med. 2009; 37:1920–9. [PubMed: 19542304]
18. Xu H, Othman SF, Magin RL. Monitoring tissue engineering using magnetic resonance imaging. J. Biosci. Bioeng. 2008; 106:515–27. [PubMed: 19134545]
19. Othman SF, Curtis ET, Plautz SA, Pannier AK, Butler SD, Xu H. MR elastography monitoring of tissue-engineered constructs. NMR Biomed. 2012; 25:452–63. [PubMed: 21387443]
20. Yin Z, Schmid TM, Yaşar TK, Liu Y, Royston TJ, Magin RL. Mechanical characterization of tissue engineered cartilage using microscopic magnetic resonance elastography. Tissue Eng. Pt. C-Meth. 2014; 20:611–9.
21. Schwartz BL, Liu Y, Royston TJ, Magin RL. Axisymmetric diffraction of a cylindrical transverse wave by a viscoelastic spherical inclusion. J. Sound Vibration. 2016; 364:222–233.
22. Ben-Menahem, A.; Singh, SJ. Seismic Waves and Sources. Springer-Verlag, Inc.; New York: 1981. p. 990
23. Morse, PM.; Feshbach, H. Methods of Theoretical Physics. McGraw-Hill Book Company, Inc.; New York: 1953. p. 1763
24. Pow, Y-H.; Mow, C-C. Diffraction of Elastic Waves and Dynamic Stress Concentrations. Crane, Russak & Company, Inc.; New York: 1973. p. 601
25. Knutsson, H.; Westin, CF.; Granlund, G. Local multiscale frequency and bandwidth estimation Image Processing.. Proceedings. ICIP-94., IEEE International Conference; Austin, TX. IEEE; 1994. p. 36-40.
26. Manduca A, Oliphant TE, Dresner MA, Mahowald JL, Kruse SA, Amromin E, Felmlee JP, Greenleaf JF, Ehman RL. Magnetic resonance elastography: non-invasive mapping of tissue elasticity. Med. Image Anal. 2001; 5:237–54. [PubMed: 11731304]
27. Graff, KF. Wave Motion in Elastic Solids. Dover Publications, Inc.; New York: 1975. p. 60
28. Kubenko VD, Savin VA. Construction of the velocity potential of a semiinfinite liquid column excited by a spherical calotte oscillating inside a cylindrical cavity. Int. Appl. Mech. 2000; 36:358–66.
29. Olsson S. Point force excitation of a thick-walled elastic infinite pipe with an embedded inhomogeneity. J. Eng. Math. 1994; 28:311–25.
30. O'Neill W, Penn R, Werner M, Thomas J. A theory of fine structure image models with an application to detection and classification of dementia. Quant. Imaging Med. Surg. 2015; 5:356–67. [PubMed: 26029638]

31. Magin, RL. Fractional Calculus in Bioengineering. Begell House; Connecticut: 2006.
32. Oldham, KBA.; Spanier, JA. The Fractional Calculus: Theory and Applications of Differentiation and Integration to Arbitrary Order. Dover Publications, Inc.; New York: 2006.

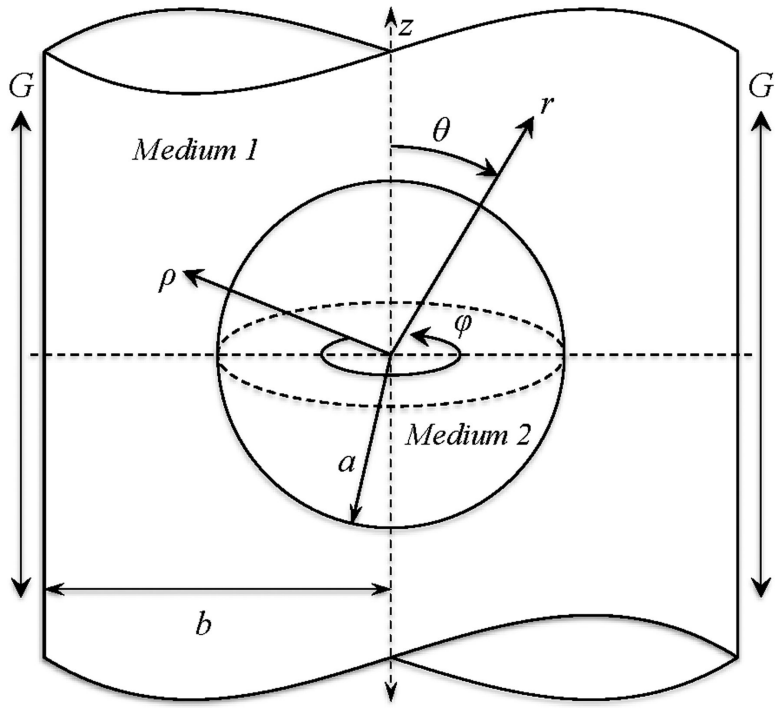

Figure 1.

The cylindrical medium, medium 1, is referred to a cylindrical coordinate system, r and z, with the z axis coinciding with the axis of medium 1. The spherical coordinates, r and θ, are assigned to the center of the spherical inclusion, medium 2.

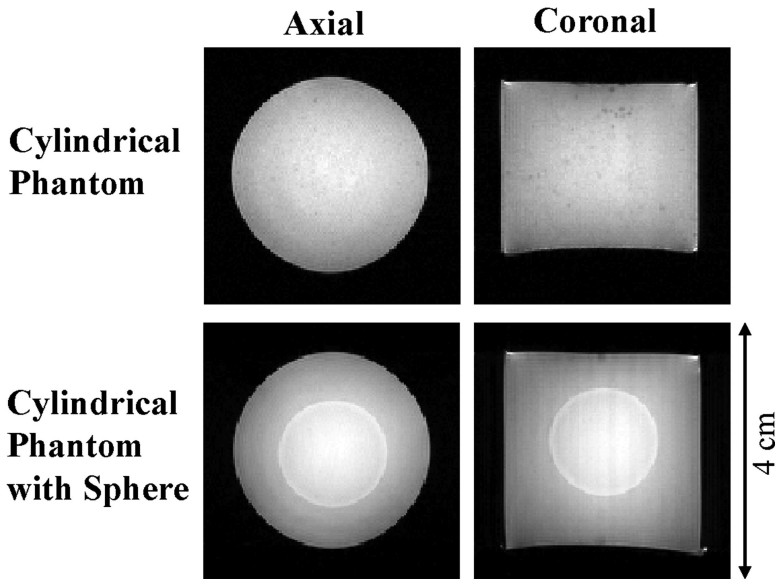

Figure 2.

Magnetic resonance magnitude images of the homogenous (top) and heterogenous (bottom) phantoms. The left column is the axial plane through the center while the right column is the coronal plane, also through the center.

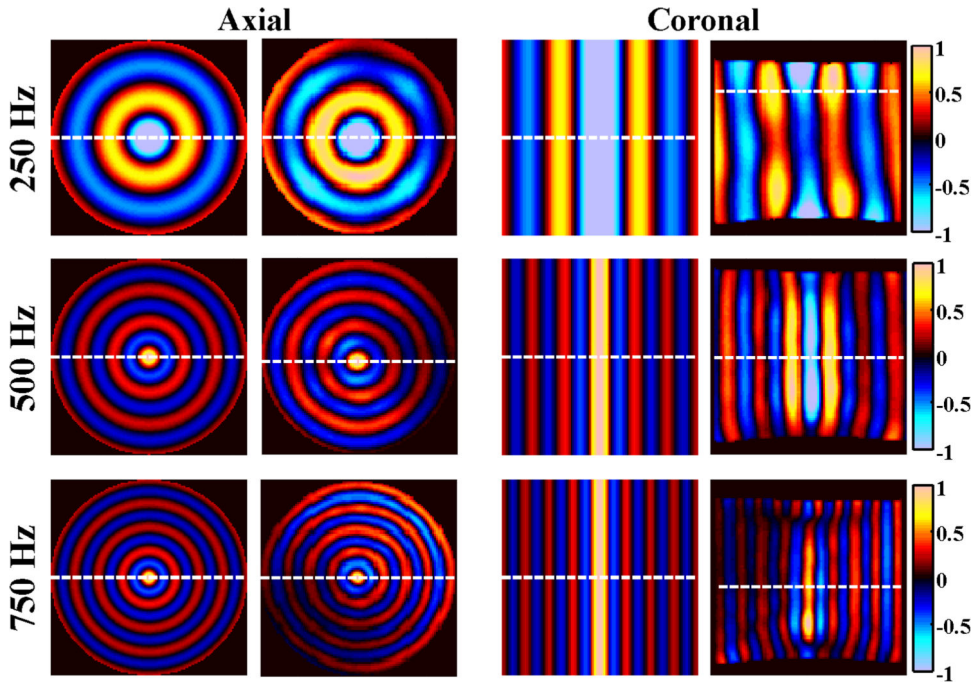

Figure 3.

Displacement wave fields from the homogenous plantom. The top, middle, and bottom rows correspond to excitation frequencies of 250, 500, and 750 Hz, respectively. The left and right pairs of columns are the axial and coronal views, each of which comprises the theoretical (left) and experimental (right) results. The color bar on the right is the normalized displacement.

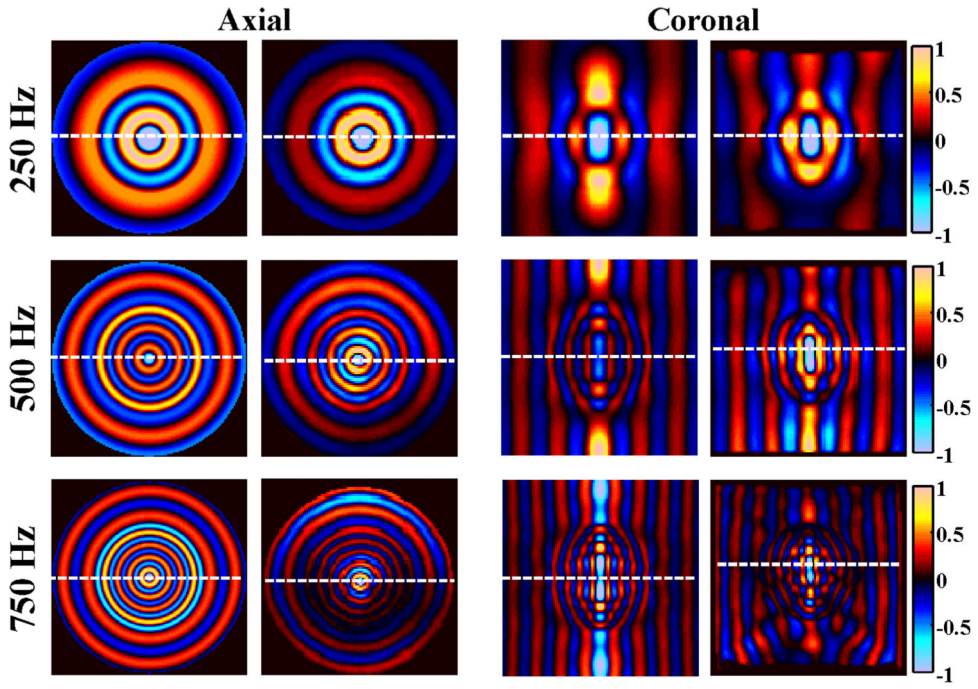

Figure 4.

Displacement wave fields from the heterogeneous phantom. The top, middle, and bottom rows correspond to excitation frequencies of 250, 500, and 750 Hz, respectively. The left and right pairs of columns are the axial and coronal views, each of which comprises the theoretical (left) and experimental (right) results. The color bar on the right is the normalized displacement.

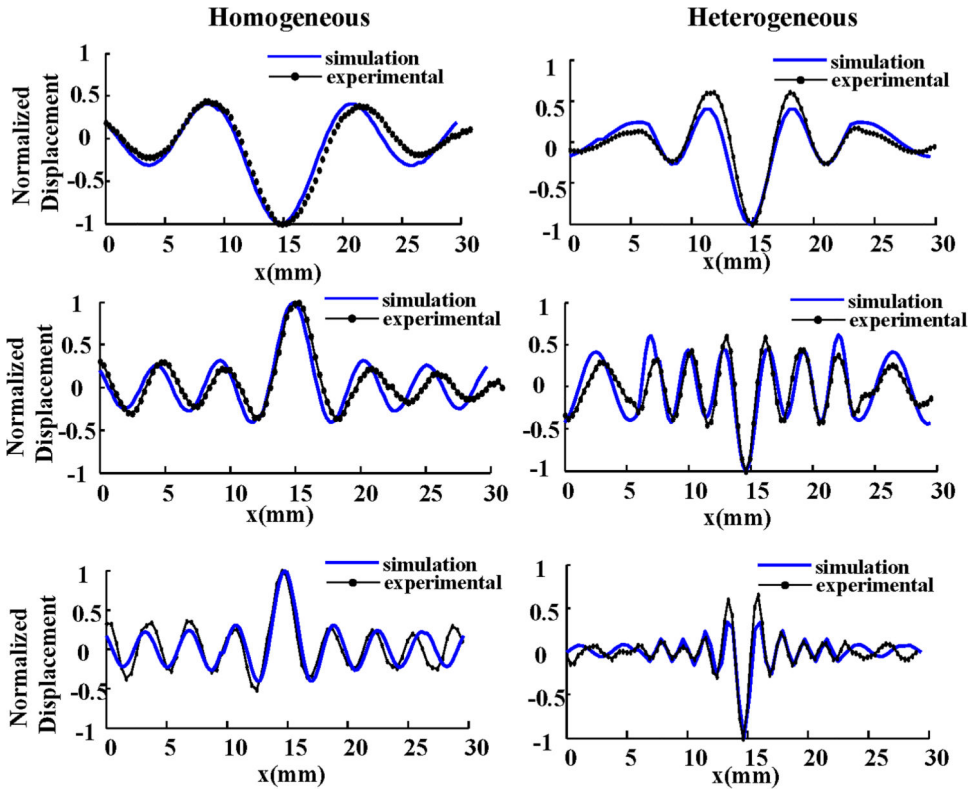

Figure 5.

Comparison of the theoretical simulation and experimental displacements along the dotted white line indicated in figure ?? and figure ??.

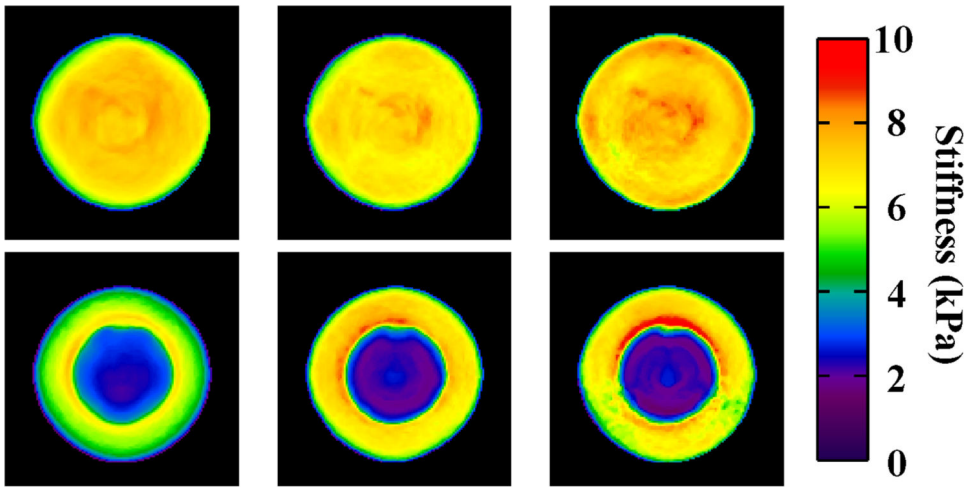

Figure 6.

Elastograms calculated using LFE from the experimentally obtained wave field through the axial plane from the homogenous (top) and heterogeneous (bottom) phantoms. From left to right the excitation frequencies are 250, 500, and 750 Hz. The color bar is storage modulus, $\Re e\mu$, and is in units of kPa.

Table 1

Complex moduli (kPa) used in the forward modeling.

Frequency	$\mathfrak{Re}\mu_1$	$\mathfrak{Im}\mu_1$	$\mathfrak{Re}\mu_2$	$\mathfrak{Im}\mu_2$
250	5.8	0.5	1.9	0.4
500	7.6	0.8	1.94	0.4
750	7.9	1.0	1.99	0.5

Table 2

Root mean squared error calculated from the line profiles in figure 5.

Frequency	Homogenous	Heterogenous
250	0.1012	0.1219
500	0.1452	0.1679
750	0.1385	0.0943